EasyChair Preprint

№ 12526

Investigation of ACFM for Metal Surface Defect Identification and Categorization

Haixu Yu, Dongping Han, Chaoyue Li and Jun Cheng

March 18, 2024

Investigation of ACFM for Metal Surface Defect Identification and Categorization

Haixu Yu, Dongping Han, Chaoyue Li, Jun Cheng
Tianjin special equipment inspection institute
Tianjin, China
yuhaixu_tjsei@163.com

Haixu Yu,Chaoyue Li
Key Laboratory of Digital Twin Generic Technology in Special Equipment for State Market Regulation
Tianjin, China

***Abstract*—The method known as Alternating Current Field Measurement, which has been extensively used in industries including petrochemicals, amusement parks, offshore platforms, and railroad transportation, has the benefits of quantitative analysis and no coating treatment. the complexity of recognizing and categorizing different types of faults since metal surfaces might have many imperfections. A parameterized scanning displacement sensor and an analysis technique for progressively extracting magnetic flux in the detecting area are presented in this research. The accuracy of simulation results is increased and the detection process is more faithfully replicated through simulation analysis. We have created models for corrosion pits, Stomas, bulges, and metal surface cracks. We have also examined the creation processes and patterns of various defect detecting signals. An experimental platform was constructed to scan and evaluate surface defects of metal specimens, and a defect detection signal recognition method was presented by comparing the patterns of various defect signals. The outcomes demonstrated the viability of this recognition technique.**

Keywords—ACFM; Simulation model; Parameterized scanning; surface defects; Identification and classification

I. INTRODUCTION

In order to find surface flaws in metal equipment, magnetic particle testing or penetration testing techniques are typically employed; however, polishing the surface beforehand raises testing expenses and decreases testing effectiveness [1-2]. By identifying magnetic signals, Alternating Current Field Measurement (ACFM) technology may examine surface fractures and flaws both qualitatively and statistically. Its benefits include not requiring polishing, being fast, and not requiring contact. These days, a lot of industries employ it, including petrochemicals, aerospace, railroad transportation, and offshore platforms.

The principle of ACFM is shown in *Fig 1*. When an alternating current signal is applied to the excitation sensor, an eddy current will be induced on the surface of the metal specimen, and the magnetic field generated by the eddy current will be uniform. When the eddy current flows through the surface open crack, it will bypass the two ends and the bottom of the crack, and then the eddy current is more dense on both sides of the crack, and the closer it is to the crack center, the more sparse it is. The magnetic field component Bx in the x direction forms peaks at both ends of the crack and a trough image at the center of the crack; The magnetic field component Bz in Z direction will form a peak and a trough image at both ends of the crack, and the magnetic field component in Y direction is not affected by defects, so it is not considered. Bx and Bz magnetic field signals contain the depth information and length information of open crack defects, and the location and size information of cracks can be obtained by analyzing the detection signals of Bx and Bz [3].

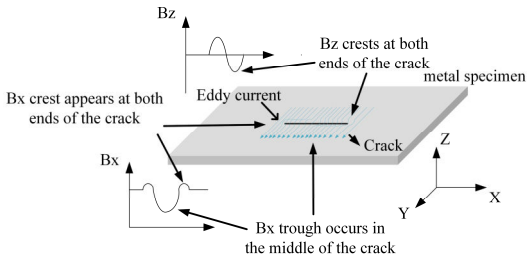

Fig 1 Schematic diagram of ACFM principle

The induced current and magnetic field distribution on the surface of the tested workpiece serve as the foundation for the ACFM technology study, and finite element simulation models allow for the direct observation of the magnetic field's spatial distribution. As a result, numerous academics have studied ACFM technology through simulation modelling analysis[4-6]. In order to get real-time feature signals, Yuan [7-8] presents energy spectrum and phase threshold determination methods based on the ACFM finite element model analysis. Part of the current simulation models simulate the excitation coil for modelling using a uniform magnetic field. In order to invert the crack length and depth, BP neural network is added to the crack size real-time inversion system. The findings demonstrate that the system's inversion error is not greater than 10%. In order to detect minor crack defects on rough surface welds, a signal gradient technique is presented. This algorithm efficiently detects small surface cracks in welds and heat affected zones, as well as improving the signal-to-noise ratio of Bz signal crack response signals. The length of RCF cracks was quantitatively calculated by Rowshandel [9–10] using an artificial neural network, based on the inverse relationship between the ACFM signal and the RCF fracture cluster length. Through trials, this method's viability was confirmed. In order to increase the accuracy of crack depth inversion, Shen [11] suggested using Bz peak to peak measurements to calculate the angle between the scanning path and the fracture. Huang [12] assessed the fracture depth by calculating the ratio of the Z and X direction

components under the rotating magnetic field. This was done by using the ACFM rotating excitation magnetic field method, which lessened the impact of the crack angle on quantitative analysis. In order to detect crack defects in pipeline inner walls with a minimal depth of 1mm, Feng [13] designed an ACFM high-precision detection probe. This probe achieved both qualitative and quantitative crack defect identification. In order to determine polynomial surfaces of Bz peak spacing and crack length, as well as polynomial surfaces of Bz peak and fracture length and crack depth. Zhao [14] employed a uniaxial sensor to measure the Bz characteristic signal. He also carried out experiments to confirm the viability of this approach. Currently, the primary goal of ACFM technology research is to identify surface flaws and cracks in metal machinery. Investigations have revealed that corrosion pits and bulging flaws, in addition to crack defects, can result in alterations to the ACFM signal [15–16]. The metal surface's variations in height and roughness can interfere with the detection signal during on-site inspection, making it more challenging for inspectors to spot flaws.

In summary, this paper establishes a three-dimensional simulation model based on ACFM principle, puts forward a model analysis method of parameterized scanning displacement sensor and gradually extracting the magnetic flux in the detection coil area, and builds an ACFM test platform for verification. The results show that the detection signal of the simulation model is consistent with the experimental signal, and the simulation model can accurately restore the actual detection process.Secondly, models of metal surface crack defects, corrosion pits, porosity defects, and bulge defects were established, and the distribution of eddy currents and magnetic fields around different defects was analyzed. Different defect signal patterns were compared, and a defect detection signal recognition method was proposed to assist in analyzing defect types, providing reference for defect signal recognition and classification in ACFM on-site inspection.

II. Creation and Analysis of Simulation Models

A. Building three-dimensional simulation models

A three-dimensional simulation model is established, as illustrated in *Fig 2*, to aid in the extraction of magnetic flux components in various directions. The multiphysics field simulation model is based on the principle of ACFM detection and visually reflects the surface magnetic field and induced current distribution of the specimen.

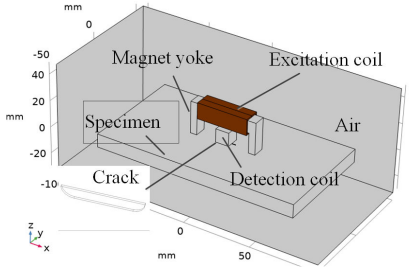

Fig 2 ACFM simulation model

The primary components of the ACFM simulation model includs winding excitation coils, excitation probe magnetic yokes, specimens with defects (surface crack defects), detection coils, and air domains. To excite the magnetic field, a sinusoidal current is fed into the winding excitation coil. The coil shape is chosen to be rectangular due to the small attenuation rate and uniform dispersion of the magnetic field produced by the coil. Because of its high magnetic permeability, the excitation probe yoke can amplify the induced current on the specimen's surface by collecting magnetic induction lines. The surface defect of the specimen is set as a crack defect, and the model is replaced by a narrow rectangular prism placed in the center of the specimen, with the defect length direction parallel to the x-axis surface. The detection coil is located directly below the excitation probe yoke to extract and analyze the magnetic flux component on the surface of the specimen. The remaining space of the model is set as the air domain, and the size parameters of the simulation model are shown in Table 1.

TABLE 1 ACFM simulation model size parameters (mm)

Model Nam	X Size	Y Size	Z Size
Specimen	150	80	10
Air domain	200	100	80
Defect	15	0.5	3
Excitation coil	12	38	12
Detection coil	10	10	10

Assign material attributes to each component of the model once the geometric model has been established. The two most crucial simulation parameters for material properties in electromagnetic simulation are conductivity and magnetic permeability. Table 2 displays the model's distinctive parameters.

TABLE 2 Model characteristic parameters

Excitation frequency	coil turns	loading current	Yoke material	specimen material
5kHz	200turns	0.1A	manganese zinc ferrite	Q235

Note: The relative magnetic permeability of manganese zinc ferrite is 7000, and the relative magnetic permeability of Q235 is 200.

The skin effect of generated current on the surface of ferromagnetic materials is evident at an excitation frequency of 5 kHz. The current is sparsely distributed internally and is mostly concentrated on the specimen's surface. To increase the speed of the calculation, impedance boundary conditions are set as the specimen boundary conditions. The size of the crack defect is set to 20mm in length, 0.5mm in width, and 3mm in depth. After setting the key parameters, grid partitioning and frequency domain calculations were performed, and the simulation results are shown in *Fig 3*.

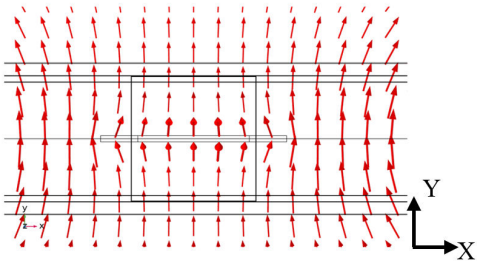

Fig 3 Simulation Results

The induced current density on the specimen's surface is depicted in *Fig 3*. The illustration shows that the current in the centre of the yoke flows along the y-axis direction, whereas the

induced current is shaped like a vortex close to the yoke. At a distance from the defect, the specimen's current distribution is uniform, with current flowing through the gap in the defect and accumulating at both ends. At both extremities of the flaw, the current deviation is pointing in the opposite direction.

The crack defects of the specimen were detected using a parameterized scanning mobile excitation probe and detection coil. The geometric center of the detection coil was gradually moved from -30mm to 30mm, with a step of 2mm. The excitation probe and detection coil perform a calculation at each position and extract the magnetic flux component at that position. The model restores the actual detection process, and the detection results are shown in *Fig 4*.

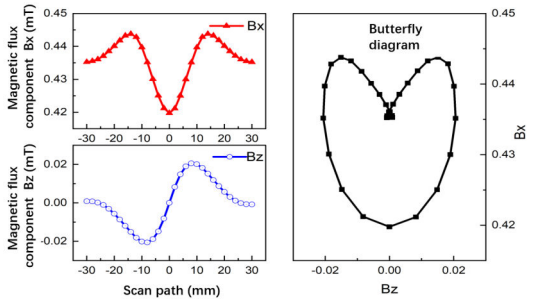

Fig4 Magnetic flux signal

Fig 4 shows two peaks and one valley in the magnetic flux curve Bx, with the peaks occurring near the crack end face and the valleys occurring at the center of the crack. The magnetic flux curve Bz first exhibits valleys and then peaks, with a spacing of 20mm between the valleys and peaks, which is the same as the crack length set on the specimen.

B. Experimental Platform Construction and Verification

As illustrated in *Fig 5*, construct an experimental platform for ACFM technology that includes a three-axis movable platform, ACFM sensors, and portable detecting equipment. The hardware elements of the portable detecting equipment in the experimental platform include a filter, dynamic memory, power amplifier, and signal generator. The equipment's embedded software performs tasks like human-computer interaction, background operations, detection algorithm compilation, and overall code optimization. The three-axis moving platform moves with a displacement accuracy of 0.1mm in the x, y, and z directions by means of a stepper motor.

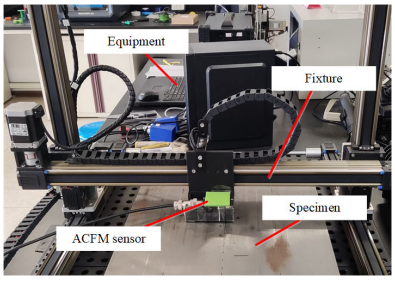

Fig5 ACFM experimental platform

The specimen is a Q235 steel plate with electrical discharge machining defects. The defect size is 20mm long, 3mm deep, and 0.5mm wide, which is the same as the defect size set in the simulation.The sensor travels at a speed of 15 mm/s and detects from 50 mm to 50 mm on the left side of the crack. The excitation signal is a 5 kHz sine signal. *Fig 6* compares the generated signal with the derived experimental test detection signal. The simulation signal result is represented by the black curve, while the experimental signal is represented by the red dot plot.The experimental data points are scattered on both sides of the generated magnetic flux curve, as shown in *Fig 6* and the experimental signal's peak and valley data points essentially coincide with the simulated signal. The computer signal and the experimental signal diverge slightly at trajectories of 20 and -30 mm. It is caused by the material's edge effect and experimental flaws, according to testing conducted through experimentation. The outcomes show that the aforementioned approach can faithfully capture the real ACFM detection procedure.

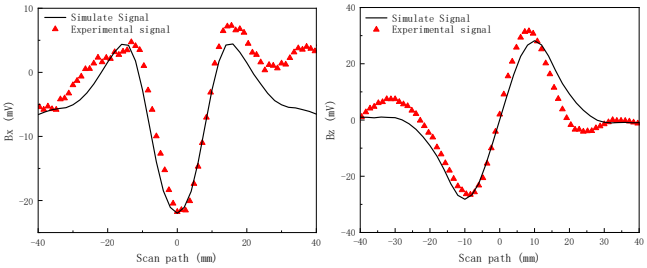

(a) Bx magnetic flux density (b) Bz magnetic flux density

Fig 6 Comparison of detection signals

III. Analysis of Metal Surface Defects

A. Establishment of Metal Defect Model

As seen in *Fig 7*, four different types of defects—cracks, corrosion pits, Stoma, and bulges—were placed at the centre of the flat plate specimen using the aforementioned simulation model and analysis technique. The size parameters of defects are shown in *Table 3*, where the size of porosity defects remains unchanged and the arrangement is 8 × 2、 4 × 2、 4 × 1.

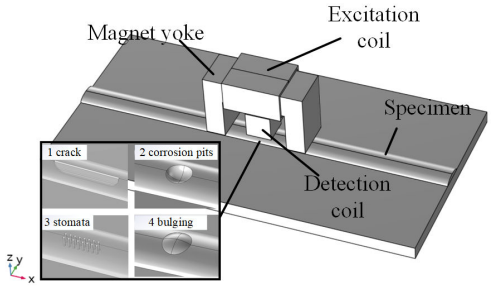

Fig 7 Surface defect model

TABLE 3 Defect Size Parameters

Defect type	Defect length L or radius R (mm)	Defect depth H (mm)
Cracks	10、20、30、40	3
Corrosion pits	2、2.5 、5	2 、3
Stoma	0.5	2
Bulging	3、4	0.5

Using frequency domain computations, determine the distribution of the spatial magnetic field and the induced current surrounding various flaws. Set the detection coil's movement

distance along the x-axis to 60 mm, moving 2 mm at a time. The magnetic flux curves Bx and Bz on the detection path are obtained by the model by doing a single calculation at each place and extracting the magnetic flux component of the detection coil area at that position.

B. Simulation Results and Analysis

In order to acquire eddy current, magnetic flux curves, and magnetic field distribution maps surrounding crack defects, simulation calculations were performed on crack defects with various settings, as illustrated in *Fig 8*. The induced current in *Fig 8(a)* runs in the direction of the y-axis and deflects when it encounters a crack flaw. The centre of the crack has sparse current, whereas the fracture's ends have dense current. The induced current density affects the magnetic flux component Bx in *Fig (8b)* and results in distortion at both ends of the fracture, where peaks emerge in the Bx curve, and valleys in the centre of the crack. *Fig 8c)* The direction of the induced current deviation has an impact on the magnetic flux component Bz. The Bz curve is formed by a valley on the left side of the crack by the clockwise induced current, and a peak on the right side by the counterclockwise induced current. *Fig 8(d)* The magnetic flux curve Bx creates dips in the crack's centre and peaks at both of its ends. *Fig (8e)* On both sides of the fracture, there are troughs and peaks seen in the Bz signal of the magnetic flux curve.

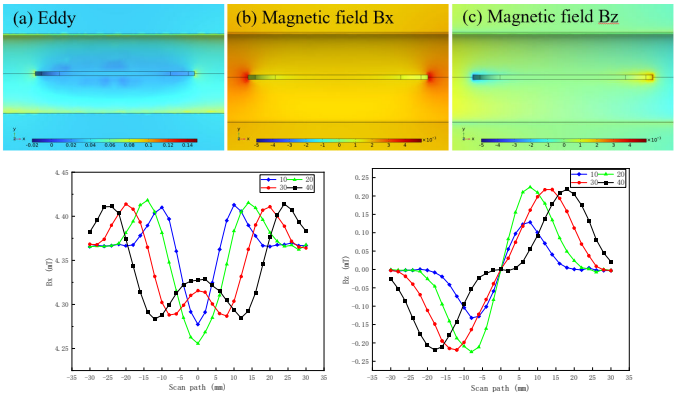

(d) Bx magnetic flux density (e) Bz magnetic flux density

Fig 8 Crack defects

Fig 9 displays the results of simulation calculations performed on corrosion pits with varying parameters. The pit defect's short current barrier range results in comparatively less current deflection in *Fig 9(a)* when compared to cracks. The magnetic field overflows at the corrosion pit's border in *Fig 9(b)*, where the magnetic field component Bx is much higher around the pit flaw than it is in the pit's centre. The specimen's x-axis magnetic field dispersion causes a magnetic field overflow in the z-axis direction on the left side of the corrosion pit in *Fig 9(c)*. The overflow magnetic field then returns to the specimen on the right side. In *Fig 9(d)* and *Fig 9(e)*, the signals of Bx and Bz exhibit distortion in proximity to the pit defect. The largest distortion happens when the magnetic yoke traverses the defect on both ends, signifying a pattern of leakage magnetic field in the detection signal. On the left side of the depression, the Bx curve initially decreases and then increases, whereas on the right side, it increases and then decreases. At a distance of around 15 mm from the moving path, the Bz curve displays a notable shift in the magnetic field signal, exhibiting a series of peaks and troughs.

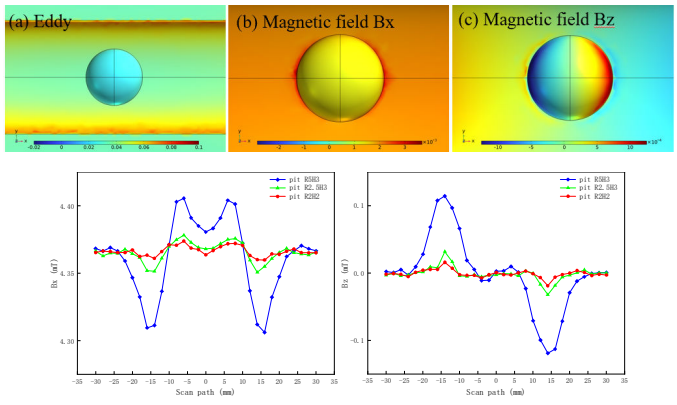

(d) Bx magnetic flux density (e) Bz magnetic flux density

Fig 9 Corrosion pit defects

Fig 10 displays the results of simulation calculations performed on stoma defect with varying parameters. Due to the small diameter of the stoma, their obstruction effect on the induced current is weak. In the eddy current distribution diagram of *Fig 10* (a), the eddy currents around the stoma are mainly distributed on both sides of the weld seam, and there is very little deviation of the eddy currents around the stoma. The magnetic field component Bx around the stoma in *Fig 10* (b) is slightly higher than the center of the stoma. The magnetic field component Bz signal in *Fig 10* (c) forms valleys and peaks on both sides of the stoma, and the background magnetic flux is affected by the magnetic yoke. The left magnetic flux is positive, and the right magnetic flux is negative. The magnetic flux curves in *Fig 10* (d) and 10 (e) exhibit multiple fluctuations at the stoma, with the smallest distortion compared to other defects.

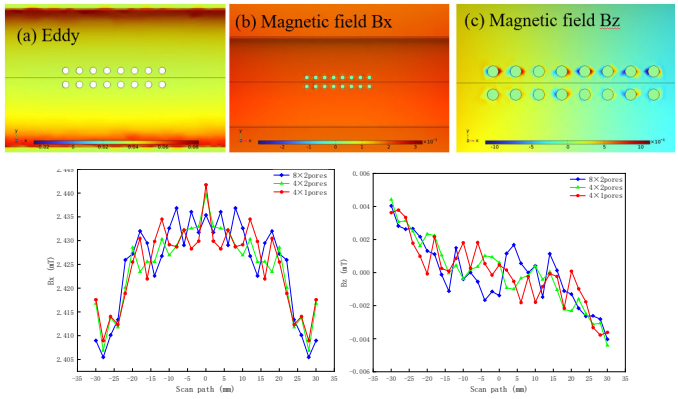

(d) Bx magnetic flux density (e) Bz magnetic flux density

Fig 10 Stoma defects

Fig 11 displays the results of simulation calculations performed on bulging defect with varying parameters. *Fig 11(a)* Local current concentration happens at both ends of the bulge along the y-direction, and Eddies are primarily concentrated on both sides of the weld seam. *Figs. 11(b)* and *11(c)* show a distinct distribution of the magnetic field than previous defect magnetic field patterns. On both sides of the bulge defect, Bx exhibits a strong magnetic field, while the magnetic field strength is weak in the centre of the defect. Bz's bulging defect

has directions that are opposite on each side. While the magnetic field signal Bz in *Fig 11(d)* first displays a trough and then a peak signal, the Bx curve in *Fig 11(e)* displays peaks on both sides of the bulge. The bulge defect is different from the other three surface defects in that the distance between the bulge and the magnetic yoke and detection coil is closer, and the induced current and magnetic field are greater on the surface of the bulge.

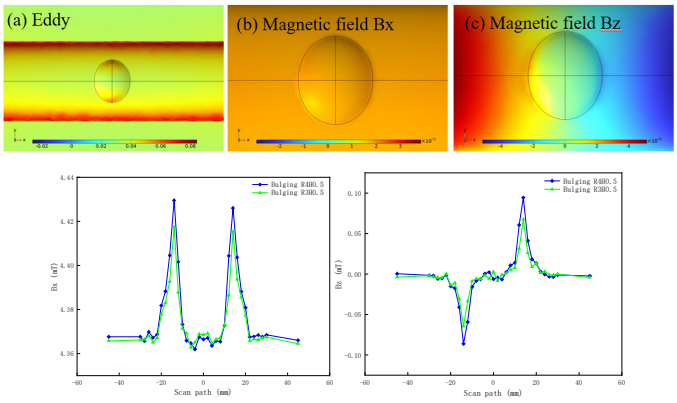

(d) Bx magnetic flux density (e) Bz magnetic flux density

Fig11 Bulging defects

C. *Defect Identification and Classification*

The variation patterns of the detection signals Bx and Bz for various kinds of flaws on the metal surface alter when the direction of the excitation coil current and the direction of sensor movement stay the same. Different types can be evaluated based on the detection signal, and *Fig 12* illustrates a potential detection signal judgment procedure to help with defect type analysis.

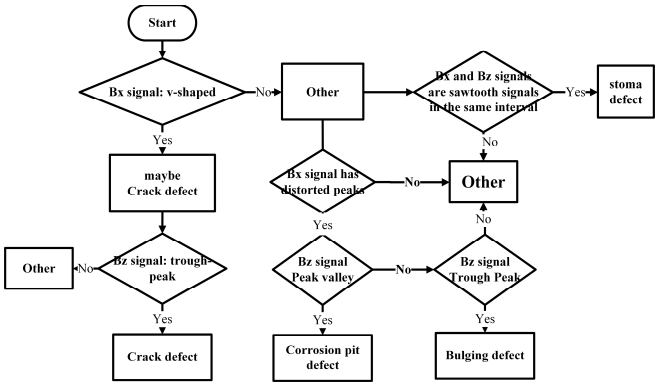

Fig 12 Classification and Identification Process of Metal Surface Defects

We used an experimental platform to scan and detect defects with manually grooved cracks and pits. The crack size parameters were: length 20 mm, width 0.5 mm, and depth 3 mm. The corrosion pit size parameters were: radius 4 mm and depth 2 mm.

The detection outcomes are displayed in Figs 13(a) and 13(c). The observed signal pattern in Fig 13(a) matches the crack defect pattern. The Bx signal shows small peaks near both ends of the crack and valleys at the centre of the fracture; the Bz signal shows valleys and peaks, respectively. In Fig 13(b), the Bz signal shows peaks and valleys along the corrosion pit's edge, while the Bx signal shows upward distortion with a peak at the corrosion pit's centre. The signal pattern complies with the pattern of corrosion pit defects, and the positive and negative peaks are in opposition to those of crack flaws. flaws can be efficiently recognized using the defect judgment procedure, and surface flaws can be found using the ACFM experimental platform.

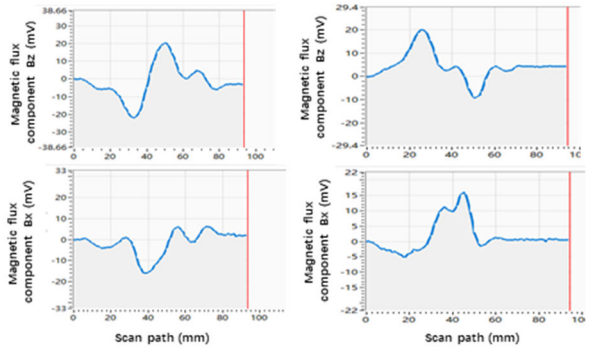

(a) crack signa (b) pit signal

Fig 13 Detection Results

IV. CONCLUSION

This paper presents an analytical approach that gradually extracts magnetic flux from the detecting coil area using parameterized scanning displacement sensors. The approach is based on the actual detection process and the ACFM concept. This approach takes into account the size of the sensor and extracts the spatial magnetic field within the detecting coil interval as the detection signal, in contrast to typical modelling methods that employ point magnetic fields as detection signals. An ACFM experimental platform was constructed in order to confirm the rules of the simulation model. The simulation results were found to be highly matched with the experimental detection signal by comparing the simulated magnetic flux signal with the experimental detection signal. This suggests that the new modelling and analysis method produces more accurate detection signals, more accurately reproduces the actual detection process of ACFM, and enhances the accuracy of the AC electromagnetic field simulation model. The establishment of the model provided a basis for the analysis of metal surface defects.

A model of metal surface crack, corrosion pit, stoma, and bulge was established through simulation, and the corresponding changes in defect detection signals were obtained. When the direction of the excitation coil current and the direction of sensor movement remain unchanged, the variation pattern of the detection signal for different defects varies. A defect detection signal recognition method was proposed by comparing different defect signal patterns to assist in analyzing defect types. The feasibility of this recognition method was demonstrated through experiments, providing reference for defect signal recognition and classification in ACFM on-site detection.

ACKNOWLEDGMENT

This work was financially supported by the Science and Technique Plan Project of State Administration for Market

Regulation (No. 2022MK011), the Science and Technique Plan Project of State Administration for Market Regulation (No. 2023MK014) and the Science and Technology Program of Tianjin Administration for Market Regulation (No. 2021-W01). Thanks to partial support for this work from Key Laboratory of Digital Twin Generic Technology in Special Equipment for State Market Regulation (Tianjin).

REFERENCES

[1] R. LeTessier, R. W. Coade, and B. Geneve, "Sizing of cracks using the alternating current field measurement technique," International Journal of Pressure Vessels and Piping, no. No.8, pp. 549-554, 2002.

[2] K. Chen, F. P. Brennan, and W. D. Dover, "Thin-skin AC field in anisotropic rectangular bar and ACPD stress measurement," NDT and E International, no. NO.5, pp. 317-323, 2000.

[3] H. Saguy and D. Rittel, "Flaw detection in metals by the ACPD technique: Theory and experiments," NDT & E International, vol. 40, no. 7, pp. 505-509, 2007.

[4] A. Akbari-Khezri, S. H. H. Sadeghi, R. Moini, and M. Sharifi, "An Efficient Modeling Technique for Analysis of AC Field Measurement Probe Output Signals to Improve Crack Detection and Sizing in Cylindrical Metallic Structures," Journal of Nondestructive Evaluation, vol. 35, no. 1, 2015.

[5] W. Zheng, L. Zhang, Y. Su, and T. Fang, "Numerical Simulation of a U-Shaped ACFM Inducer," Materials Transactions, vol. 56, no. 5, pp. 743-748, 2015.

[6] L. Wei, C. Guoming, L. Wenyan, L. Zhun, and L. Feng, "Analysis of the inducing frequency of a U-shaped ACFM system," NDT & E International, vol. 44, no. 3, pp. 324-328, 2011.

[7] G. L. Nicholson, H. Rowshandel, X. J. Hao, and C. L. Davis, "Measurement and modelling of ACFM response to multiple RCF cracks in rail and wheels," Ironmaking & Steelmaking, vol. 40, no. 2, pp. 87-91, 2013.

[8] H. Rowshandel, G. L. Nicholson, J. L. Shen, and C. L. Davis, "Characterisation of clustered cracks using an ACFM sensor and application of an artificial neural network," NDT & E International, vol. 98, pp. 80-88, 2018.

[9] W. Li et al., "Real-time and high-precision cracks inversion algorithm for ACFM based on GA-BP neural network," Zhongguo Shiyou Daxue Xuebao (Ziran Kexue Ban)/Journal of China University of Petroleum (Edition of Natural Science), no. No.5, pp. 128-134, 2016.

[10] X. Yuan et al., "Identification of Tiny Surface Cracks in a Rugged Weld by Signal Gradient Algorithm using the ACFM Technique," Sensors (Basel), vol. 20, no. 2, Jan 9 2020.

[11] J. L. Shen, L. Zhou, H. Rowshandel, G. L. Nicholson, and C. L. Davis, "Determining the propagation angle for non-vertical surface-breaking cracks and its effect on crack sizing using an ACFM sensor," Measurement Science and Technology, vol. 26, no. 11, 2015.

[12] R. Huang, M. Lu, Z. Chen, and W. Yin, "Reduction of Coil-Crack Angle Sensitivity Effect Using a Novel Flux Feature of ACFM Technique," 2021.

[13] Y. Feng, H. Liu, L. Zhang, and W. Zheng, "In-line inspection technology of oil and gas long-distance pipeline based on alternating current field measurement," TM-TECHNISCHES MESSEN, no. No.4, pp. 256-265, 2023.

[14] S. Zhao, L. Sun, J. Gao, J. Wang, and Y. Shen, "Uniaxial ACFM detection system for metal crack size estimation using magnetic signature waveform analysis," Measurement, vol. 164, 2020.

[15] X. Yuan，et al.， "Visual Reconstruction of Irregular Crack in Austenitic Stainless Steel Based on ACFM Technique," Journal Of Mechanical Engineering, vol. 10, pp. 27-33, 2020.

[16] J. Zhao, W. Li, J. Zhao, X. a. Yuan, Y. Zhu, and Z. Wang, "A Novel ACFM Probe With Flexible Sensor Array for Pipe Cracks Inspection," IEEE Access, vol. 8, pp. 26904-26910, 2020.